

Cosmic Flow Measurement and Mock Sampling Algorithm of Cosmicflows-4 Tully-Fisher Catalogue

FEI QIN,^{1,*} DAVID PARKINSON,¹ CULLAN HOWLETT,² AND KHALED SAID²

¹*Korea Astronomy and Space Science Institute, Yuseong-gu, Daedeok-daero 776, Daejeon 34055, Republic of Korea.*

²*School of Mathematics and Physics, The University of Queensland, Brisbane, QLD 4072, Australia.*

(Received June 1, 2019; Revised January 10, 2019; Accepted October 1, 2021)

Submitted to ApJ

ABSTRACT

Measurements of cosmic flows enable us to test whether cosmological models can accurately describe the evolution of the density field in the nearby Universe. In this paper, we measure the low-order kinematic moments of the cosmic flow field, namely bulk flow and shear moments, using the Cosmicflows-4 Tully-Fisher catalogue (CF4TF). To make accurate cosmological inferences with the CF4TF sample, it is important to make realistic mock catalogues. We present the mock sampling algorithm of CF4TF. These mock can accurately realize the survey geometry and luminosity selection function, enabling researchers to explore how these systematics affect the measurements. These mocks can also be further used to estimate the covariance matrix and errors of power spectrum and two-point correlation function in future work. In this paper, we use the mocks to test the cosmic flow estimator and find that the measurements are unbiased. The measured bulk flow in the local Universe is 376 ± 23 (error) ± 183 (cosmic variance) km s⁻¹ at depth $d_{\text{MLE}} = 35$ Mpc h^{-1} , to the Galactic direction of $(l, b) = (298 \pm 3^\circ, -6 \pm 3^\circ)$. Both the measured bulk and shear moments are consistent with the concordance Λ Cold Dark Matter cosmological model predictions.

Keywords: cosmology, galaxy surveys — large-scale-structure — surveys

1. INTRODUCTION

Observations of galaxies indicate that there are fluctuations in the density field of local Universe (Jarrett 2004 and references therein). The gravitational effects of the density perturbations exert additional velocity components to the galaxies' Hubble recessional velocities, called 'peculiar velocities'. These peculiar velocities are good probes of the density field, enabling us to constrain cosmological parameters and test cosmological models.

Due to the peculiar motions of galaxies, the apparent (or inferred) distance of a galaxy, d_z is different from its true comoving distance, d_h . This difference is measurable, and quantified by the 'logarithmic distance ratio' for that galaxy, defined as

$$\eta \equiv \log_{10} \frac{d_z}{d_h}. \quad (1)$$

The η of late-type galaxies can be measured from the Tully-Fisher relation (Tully & Fisher 1977; Strauss & Willick 1995; Masters et al. 2008; Hong et al. 2014), while for early-type galaxies, η can be measured from the Fundamental Plane (Djorgovski & Davis 1987; Dressler et al. 1987; Strauss & Willick 1995; Magoulas et al. 2012; Springob et al. 2014; Said et al. 2020; Howlett et al. 2021 in prep). The peculiar velocity of a galaxy can be estimated from its log-distance ratio using velocity estimators (Davis & Scrimgeour 2014; Watkins & Feldman 2015; Adams & Blake 2017).

The cosmic flow field in the local Universe arises from the peculiar velocities of galaxies. Measuring the low-order kinematic moments of the cosmic flow field, i.e. bulk flow and shear moments, from peculiar velocity surveys and comparing them to the Λ Cold Dark Matter theory predictions enables us to test whether the theory accurately describe the motion of galaxies on large scales. In previous work, the bulk and shear moments are commonly measured using two different methods: maximum likelihood estimation (MLE, Kaiser 1988); minimum variance (MV) estimation (Watkins et al. 2009; Feldman et al. 2010). The measurements generally agree so far with the Λ cold dark matter model (Λ CDM)

Corresponding author: Fei Qin
feiqin@kasi.re.kr

* Korea Astronomy and Space Science Institute, Yuseong-gu, Daedeok-daero 776, Daejeon 34055, Republic of Korea.

prediction (Kaiser 1988; Staveley-Smith & Davies 1989; Jaffe & Kaiser 1995; Nusser & Davis 1995; Parnovsky et al. 2001; Nusser & Davis 2011; Turnbull et al. 2012; Ma & Scott 2013; Ma & Pan 2014; Hong et al. 2014; Scrimgeour et al. 2016; Qin et al. 2018, 2019b; Boruah et al. 2020; Qin 2021; Stahl et al. 2021).

In this paper we will measure the bulk flow and shear moments using the peculiar velocity catalogue, Cosmicflows-4 Tully-Fisher catalogue (CF4TF, Kourkchi et al. 2020b), and compare the measurements to the Λ CDM predictions to test the model. CF4TF is the currently largest full sky catalogue of Tully-Fisher galaxies, enables us to more accurately measure the bulk and shear moments and the measurements are less affected by the an-isotropic sky coverage, comparing to previous work.

In addition, as CF4TF is one of the key components of the future full Cosmicflows-4 catalogue, we present the mock sampling algorithm for CF4TF in this paper. Combining these CF4TF mocks with the 6dFGSv mocks (Qin et al. 2018, 2019a), we can obtain mock catalogues for the two largest subsets of the final full Cosmicflows-4 catalogue. Our mocks can model the luminosity selection, survey geometry of the real surveys, enabling researchers to explore how these systematics affect the measurements (Qin et al. 2018, 2019b; Howlett et al. 2021 in prep). In future work, these mocks can be used to study the power spectrum and two-point correlation of velocities of Cosmicflows-4 catalogue. They are the key to estimate the covariance matrix and errors of these measurements. They can also be used to test the methods of these measurements to identify any possible biases. The mock catalogues underlying this article will be shared on a reasonable request to the corresponding author. In this paper, these mock are used to test the cosmic flow (bulk and shear moments) estimator to explore how well the estimator recover the true moments.

The paper is structured as follows: in Section 2, we introduce the CF4TF data. In Section 3, we introduce the L-PICOLA simulation (Howlett et al. 2015a,b) and present the mock sampling algorithm. In Section 4, we introduce the cosmic flow estimator and test the estimator using mocks. We present the final results and discussion in Section 5. A conclusion is presented in Section 6.

We adopt a spatially flat Λ CDM cosmology as the fiducial model. The cosmological parameters are: $\Omega_m = 0.3121$, $\Omega_\Lambda = 0.6825$ and $H_0 = 100 h \text{ km s}^{-1} \text{ Mpc}^{-1}$ with $h = 0.6751$.

2. DATA

The Cosmicflows-4 Tully-Fisher catalogue (CF4TF, Kourkchi et al. 2020b) is a full-sky catalogue of 9790 galaxies. The sky coverage of the CF4TF galaxies under Galactic coordinates is shown in Fig.1. The redshift of the CF4TF galaxies reaches 20000 km s^{-1} , the redshift distribution is

shown in Fig.2. The distances of galaxies are measured using the Tully-Fisher relation (Tully & Fisher 1977; Kourkchi et al. 2020b), which is a linear relation between the H I rotation widths and photometry magnitudes.

The H I data is taken from the following four catalogues. The primary catalogue is the All Digital H I catalogue (ADHI, Courtois et al. 2009), the galaxies with H I line widths uncertainties $\leq 20 \text{ km s}^{-1}$ are selected. In the ADHI, the galaxies below declination $\delta = -45^\circ$ are observed by the Parkes Telescope (Courtois et al. 2011), the number density of galaxies is lower in this region. Most of the remainder is the Arecibo Legacy Fast ALFA Survey (ALFALFA, Haynes et al. 2018, 2011), mainly distributed in declination range of $[0^\circ, 38^\circ]$ and the galaxies with H I spectrum signal-to-noise ratio $\text{SNR} > 10$ are selected. The rest are the Springob/Cornell catalog (Springob et al. 2005) and the Pre-Digital H I catalog (Fisher & Tully 1981; Huchtmeier & Richter 1989).

The u, g, r, i and z bands photometry is taken from the Sloan Digital Sky Survey (SDSS) Data Release 12 (DR12, York et al. 2000). The w_1 and w_2 bands data is taken from the Wide-field Infrared Survey Explorer (WISE, Wright et al. 2010). The i-band absolute magnitude cut $M_i \leq -17 \text{ Mag}$ is applied to the data (Kourkchi et al. 2020b,a).

3. MOCKS

3.1. L-PICOLA simulation

Producing realistic mock surveys that model non-linear gravitational interactions requires N-Body simulations. However, such full N-body simulations, which model the gravitational forces and motions down to a fine resolution, can require an extensive HPC infrastructure and a large amount of CPU-time. To make a large-ensemble of mock surveys quickly and efficiently, we use the COmoving Lagrangian Acceleration (COLA) approach (Tassev et al. 2013) implemented in the L-PICOLA code (Howlett et al. 2015a,b).

We use L-PICOLA to generate 250 dark matter simulations. Though approximate, this method and code have been demonstrated to reproduce the clustering of dark matter particles and halos well on all scales of interest for galaxy and peculiar velocity clustering (Howlett et al. 2015a,b; Blot et al. 2019), at $\geq 95\%$ accuracy for both the power spectrum and bispectrum at $k = 0.3 h \text{ Mpc}^{-1}$. Halos are identified in these simulations using the 3D Friends-of-friends algorithm in the VELOCIRaptor code (Elahi 2009). This code has also been demonstrated to recover realistic halos, subhalos and halo merger trees (although we only the the first of these here), in agreement with a variety of other halo-finders (Onions et al. 2012; Knebe et al. 2013).

The fiducial cosmology is given by $\Omega_m = 0.3121$, $\Omega_b = 0.0488$, $\sigma_8 = 0.815$, and $h = 0.6751$. The redshift of the simulations is at $z = 0$. The boxsize is 1800 Mpc h^{-1} . The

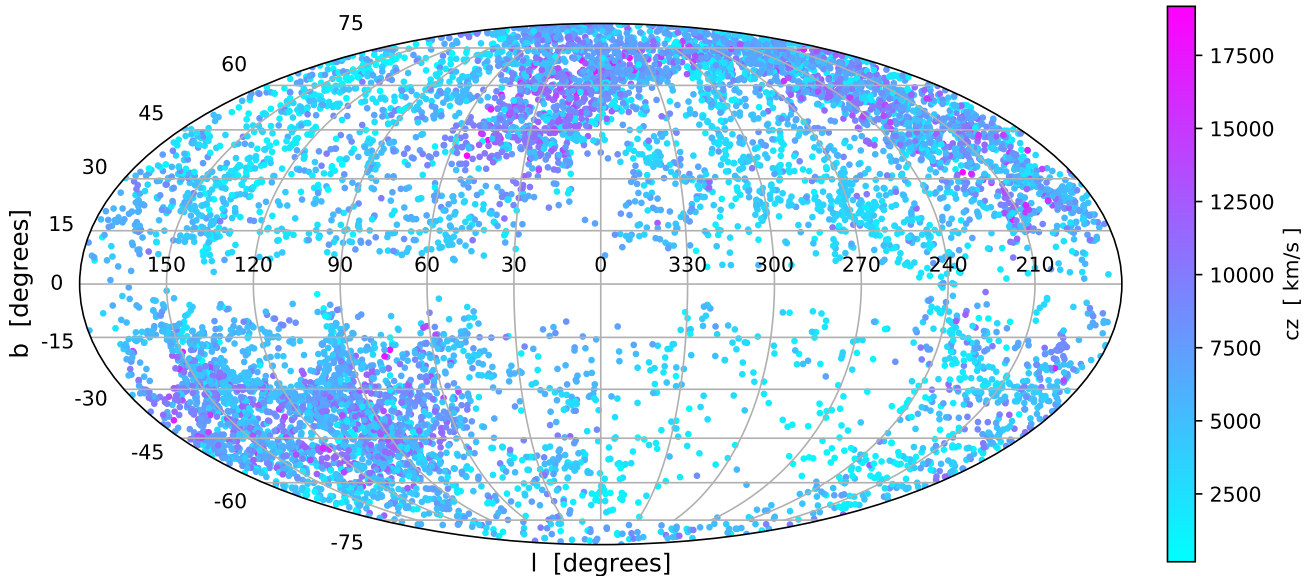


Figure 1. The sky coverage of the CF4TF galaxies under Galactic coordinates. The colors of the dots represent the redshift of the galaxies, according to the color bar.

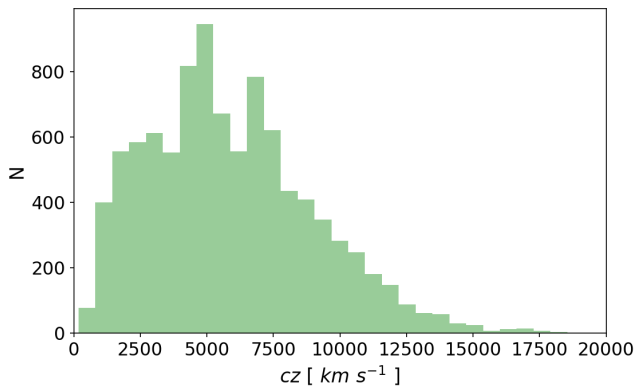


Figure 2. The redshift distribution of the CF4TF galaxies.

number of particles in each simulation is 2560^3 . The minimum halo mass is $\sim 5 \times 10^{11} M_{\odot} h^{-1}$ (20 particles per halo).

3.2. Mock sampling algorithm for CF4TF

We have 250 simulation boxes in total, each simulation provides us with the mass m_{hl} of halos, Cartesian positions $[x, y, z]$ and velocities $[v_x, v_y, v_z]$ of halos. We divide each simulation box into eight identical sized cubes. In each cube, the observer is placed at a galaxy close to the center of that cube. Therefore, we have generated 2000 mock CF4TF catalogues in total.

The halos in the simulations are parent halos, it is required to generate subhalos and galaxies from these parent halos. The starting point is the halo concentration, defined as

$$c_v \equiv \frac{r_v}{r_s} \quad (2)$$

which characterises the mass distribution in a halo. r_v is the virial radius of a halo. r_s is the break radius between an inner and outer density profile in a halo. c_v is computed purely as a function of parent halo mass m_v using the fitted relationship from Prada et al. (2012), calibrated on high resolution N-body simulations. The virial radius is also computed using the parent halo mass and assuming the halo is both spherical and has a density $200\times$ the critical density of the Universe. Given c_v and r_v , one can generate the subhalos and galaxies using the Navarro–Frenk–White (NFW) profile (Navarro et al. 1997).

The subhalo generation algorithm is based on Vale & Ostriker 2004; Conroy et al. 2006; Howlett et al. 2015c, 2017; Qin et al. 2019a and detailed below:

1. First, we assume a power law distribution for the mass ratio between a subhalo and its parent halo. From this power law distribution, we can compute the expected number of subhalos as

$$\lambda_{Poi} = \int_{f_{min}}^1 A f_M^{-\alpha_h} df_M \quad (3)$$

where f_M is the mass ratio between the subhalo and its parent. f_{min} is the minimum mass ratio we consider, which we set, based on the minimum halo mass of the simulation (see Section 3.1), to 20 times the dark matter particle mass divided by the parent halo mass (i.e., a fixed minimum mass, such that the minimum mass *ratio* varies based on the parent halo). The free parameters A and α_h will be fitted by matching the density power spectrum of mocks to real data.

2. To add realism to the sampling process, the actual number of subhalos in each parent halo N_{sub} is generated assuming a Poisson distribution with mean λ_{Poi} . The mass ratios

of the N_{sub} subhalos are generated by drawing uniform random numbers in the interval $[0, 1]$, and inverting the quantile distribution for Eq. 3. This results in mass ratios in the interval $[f_{min}, 1]$. The subhalo’s masses are then obtained by multiplying the set of f_M by the mass of the parent halo. As the largest value of f_M generated for the N_{sub} subhalos is 1, the masses of the subhalos will not be larger than their parent halos.

3. The positions of subhalos are generated from the NFW profile following the arguments in [Robotham & Howlett 2018](#), and rely on the concentration and virial radius for each parent halo computed as described previously. We generate N_{sub} random numbers in the interval $R \in [0, 1]$, then calculate the position parameter ([Robotham & Howlett 2018](#))

$$p = R \left(\ln(1 + c_v) - \frac{c_v}{1 + c_v} \right) \quad (4)$$

and the radius

$$r = -\frac{r_v}{c_v} \left(1 + \frac{1}{W_0(-e^{-p-1})} \right) \quad (5)$$

which gives the radial position of the subhalos relative to the center of their parent halo. Here W_0 is the Lambert Function¹. Generating N_{sub} random numbers in the intervals $[-\pi, \pi]$ and $[0, 2\pi]$ as the polar coordinates of the subhalos, respectively. Then we convert r into Cartesian coordinates using the polar coordinates. Finally we add them to the Cartesian positions of their parent halo and subtract the observer’s position to obtain the final positions of subhalos.

4. The velocities of subhalos are calculated from ([Navarro et al. 1997](#); [Howlett et al. 2015c](#))

$$v = \sqrt{\frac{Gm_v s}{r_v}} \quad (6)$$

where G is the Newton Gravitational Constant and s is the ratio between the velocities of subhalos and circular velocity of their parent halo, given by ([Navarro et al. 1997](#); [Howlett et al. 2015c](#))

$$s = \frac{1}{q} \frac{\ln(1 + c_v q) - \frac{c_v q}{1 + c_v q}}{\ln(1 + c_v) - \frac{c_v}{1 + c_v}} \quad (7)$$

Then we randomly draw the Cartesian components of the velocities v_x , v_y and v_z for the subhalos from the Gaussian function with mean equals to the velocity of their parent halo and standard deviation (std) equals to $v/\sqrt{3}$ ([Howlett et al. 2015c](#)).

5. The i-band absolute magnitude is generated using the luminosity function (see [Appendix A](#) for more discussion about

the i-band luminosity function). We re-order these magnitudes in descending order, then assign them to the halos (both parent and subhalos) in descending order of mass. We add additional scatter in this one-to-one assignment via a standard deviation parameter σ_{logM} to account for the expected scatter between halo/sub-halo mass and galaxy luminosity. This is used to draw a “proxy” luminosity for the pairwise-matching of halo mass and luminosity using a Gaussian centred on the actual simulated luminosity. Note that this “proxy” is used only for the matching, the simulated luminosity is the one actually stored and used for later applications of the mocks. Then, we obtain mock galaxies. The normalization factor ϕ_* of luminosity function will be fitted by matching the density power spectrum of mocks to real data.

6. We calculate the sky completeness of the CF4TF survey by splitting into 5 distinct patches (see, [Appendix B](#)) and comparing to the 2M++ redshift survey ([Lavaux et al. 2010](#)). To do this, the CF4TF and 2M++ are gridded using HEALPix ([Zonca et al. 2019](#); [Górski et al. 2005](#)). For each HEALPix pixel, we then calculate the ratio of galaxies in CF4TF and 2M++, treating this as the completeness. However there are two caveats to this. First, 2M++ is not quite uniform, it is 1 K -band magnitude deeper in the SDSS and 6dF regions, which we correct by normalising the sum of the values in the HEALPix pixels in these regions to be the same. Second, we would not expect every galaxy with a redshift in 2M++ to be capable of providing a TF distance. However, as we are only interested in measuring the completeness of the CF4TF measurements in one region of the sky relative to other regions, the completeness ratio is then normalized such that the mean completeness of the two patches containing ALFALFA data is one. If the completeness of a pixel is greater than one, it is set to be one.

We note that this doesn’t give an absolute measure of completeness (i.e., given all the galaxies which *could* have TF measurements in a region of the real Universe, how many actually *have* measurements in CF4TF), but it does provide a relative measure, which is all that is needed for the mocks given the following steps. Importantly, this procedure removes any signatures of large-scale structure from the completeness mask, as these structures should be present in both CF4TF and 2M++.

7. For each mock, the simulated galaxies are sub-sampled to match the smoothed redshift distribution of CF4TF data in each of the five distinct sky patches separately. Given the relative sky completeness above, this downsampling ensures the mocks have comparable numbers of objects to those we actually have TF measurements for, and that the completeness in both the angular and radial coordinates is representative of the real Universe.

¹ We use PYTHON function `scipy.special.lambertw`.

Table 1. The best fit values of the parameters used in the mock sampling algorithm.

A	α_h	$\sigma_{\log M}$	ϕ_\star
2.882	0.102	2.121	0.005

8. In a given redshift bin of the real CF4TF data, we use the Gaussian kernel distribution function² (KDE) to smooth the distribution of ϵ (denotes the measurement error of log-distance ratio η) of that redshift bin. Then we calculate the spline cumulative distribution function (CDF) from the Gaussian KDE for ϵ of that redshift bin. The spline CDF is used to generate measurements errors of log-distance ratios for mock galaxies of that redshift bin. We repeat this step for all the other redshift bins to obtain the measurements errors of log-distance ratio ϵ_{mock} for all mock galaxies.

9. The measured log-distance ratio for each mock galaxy is generated using a Gaussian function centred on the true log-distance ratio η_t with standard deviation ϵ_{mock} .³ As the measured log-distance ratios are centred on the true values, our mocks do not reproduce possible systematics such as Malmquist bias that may affect the real data. To do so would require instead simulating the observed quantities of the Tully-Fisher relationship, and running these through the same pipeline/fitting procedure as the real data. However, such a procedure was already performed when obtaining the CF4-TF data in Kourkchi et al. (2020b), so here we assume the Malmquist bias in the data has been corrected for appropriately, and the mocks only need to reproduce the remaining effects of cosmic variance and measurement errors.

10. Finally, we can measure the redshift-space density power spectrum of the 2000 mocks using the method⁴ in Howlett 2019 and Qin et al. 2019a. As shown in Fig.3, by comparing the average of these measured power spectrum (blue curve) to the density power spectrum of the real CF4TF data (black filled squares) to find the best values for the parameters A , α_h , $\sigma_{\log M}$ and ϕ_\star , as presented in Table 1. The

² We use the PYTHON package `scipy.stats.gaussian-kde`.

³ The true log-distance ratio of a mock galaxy is given by $\eta_t = \log_{10} \frac{D_m}{D_h}$, where D_h is calculated from the true position of the mock galaxy. D_m is calculated from its ‘observed’ redshift z_m , given by $z_m = (1 + z_t)(1 + v_t/c) - 1$ where z_t is the true redshift calculated from the true position. v_t is the true line-of-sight velocity of the mock galaxy calculated from its true position and velocity.

⁴ In this method, the galaxies are gridded in using their observed redshifts, then using Eq.(2.1.3) of Feldman et al. 1994 and Eq.6 of Bianchi et al. 2015 as well as Eq.11 of Yamamoto et al. 2006 to estimate the density power spectrum. This means that we are measuring the redshift-space rather than real-space power spectrum, which would need to be accounted for if we were performing any theoretical modelling, but avoids the impact of Malmquist bias or other biases that would arise if one were using the true distance to place the galaxies on the grid.

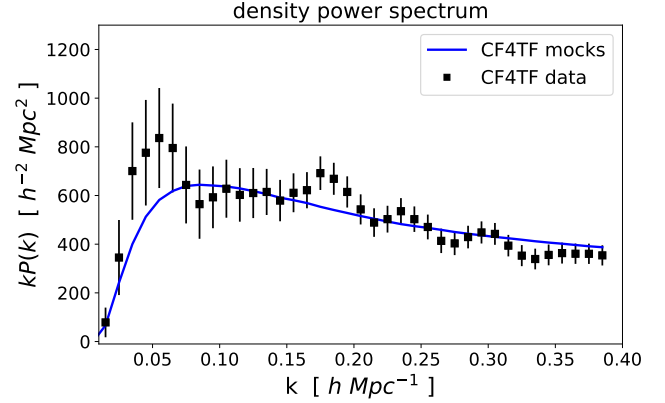


Figure 3. Comparing the density power spectrum of mocks to data. The blue curve is the average of the density power spectrum of 2000 mocks. The black filled squares are the density power spectrum measured from the real CF4TF data. The $\chi^2/d.o.f$ between the data and mock average is 39/34.

$\chi^2/d.o.f = 39/(38 - 4)$ indicates that the mocks are in excellent agreement with the data.

Fig.4 shows the comparison between the real CF4TF data and the mocks. The top left-hand-side panel shows the i-band absolute magnitude distribution. The black curve is the average of 2000 mocks, the shaded areas indicate the 1σ , 2σ and 3σ region. Here σ denotes the standard deviation of the magnitudes distributions of the 2000 mocks. The dashed blue curve is for the real CF4TF data. The top right-hand-side panel shows the distribution of the log-distance ratio for the data and mock average. The bottom left-hand-side panel shows the distribution of the error of log-distance ratio for the data and mock average. The bottom right-hand-side panel shows the redshift distribution of the data and mock average. In Fig.5, the top panel shows the sky coverage of an example mock under equatorial coordinates. For comparison, the bottom panel shows the sky coverage of the real CF4TF data under equatorial coordinates. The color of the dots indicates the redshift based on the color bars.

The mocks are in good agreement with the data. They will be continuously updated based on the updates of the real CF4TF catalogue and L-PICOLA simulations.

4. BULK AND SHEAR MOMENTS MEASUREMENTS

4.1. Bulk and shear moments

Using the Taylor series expansion, the line-of-sight peculiar velocity field, $v(d_h)$ can be expanded to the first-order (Jaffe & Kaiser 1995; Parnovsky et al. 2001; Feldman & Watkins 2008; Feldman et al. 2010; Qin et al. 2019b)

$$v(d_h) = \sum_{p=1}^9 U_p g_p(d_h), \quad (8)$$

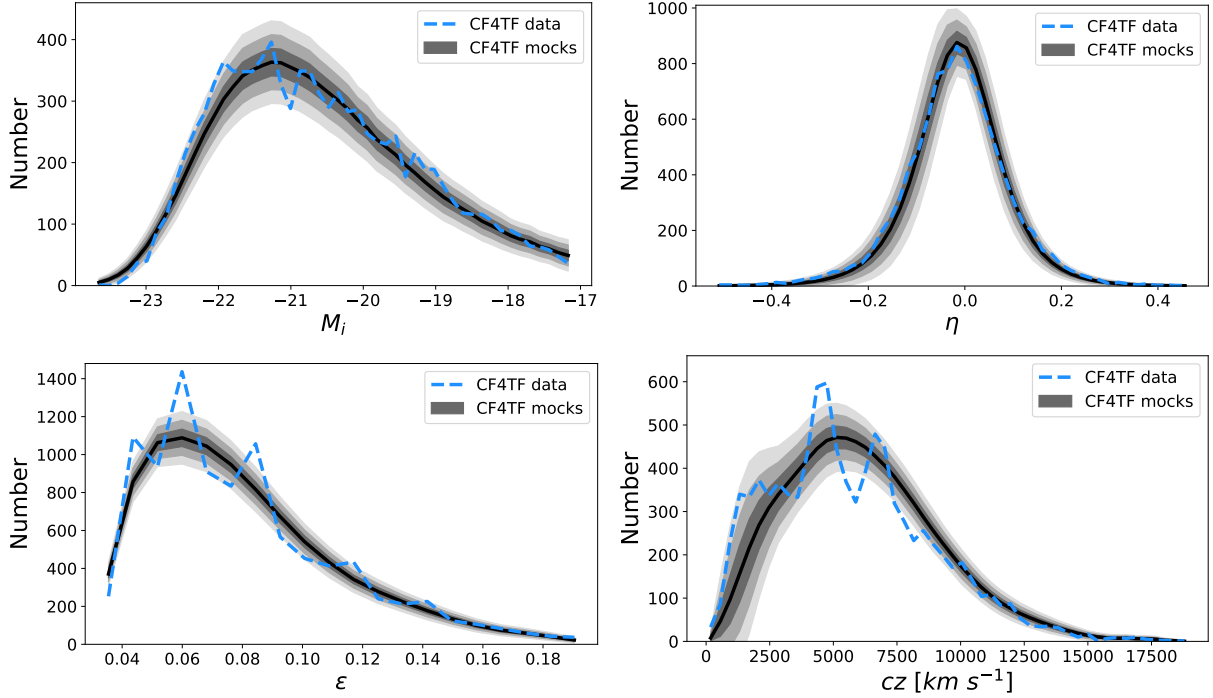


Figure 4. Comparing the mock averages (black curves) to the real CF4TF data (blue dashed curves). The shade areas indicate the 1σ , 2σ and 3σ region. The top panels are for the distribution of i -band absolute magnitudes and log-distance ratio, respectively. The bottom panels are for the distribution of errors of log-distance ratios and the redshift, respectively.

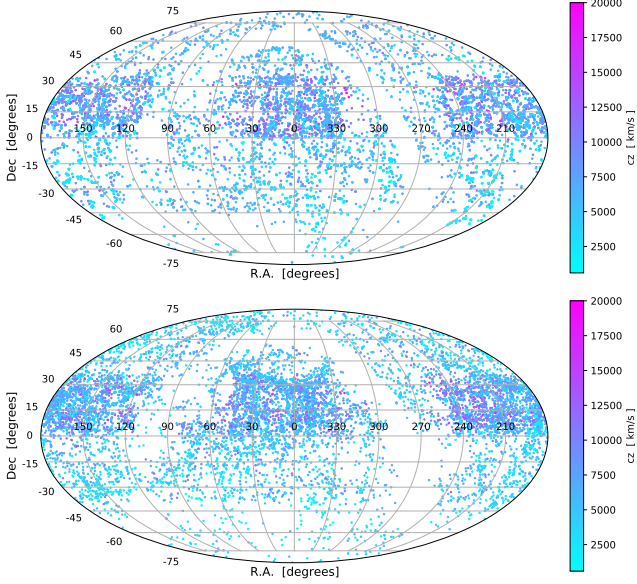


Figure 5. The top panel shows the sky coverage of an example mock under equatorial coordinates. The bottom panel shows the sky coverage of the CF4TF data under equatorial coordinates. The color of the dots represent the redshift of galaxies based on the color bars.

where U_p are the nine moment components

$$U_p = \{B_x, B_y, B_z, Q_{xx}, Q_{yy}, Q_{zz}, Q_{xy}, Q_{xz}, Q_{yz}\}, \quad (9)$$

and where the zeroth-order vector $[B_x, B_y, B_z]$ is the so called bulk flow velocity. The first-order symmetric tensor Q_{ij} , ($i, j = x, y, z$) is the so called shear moment. The mode functions are given by

$$g_p(d_h) = \{\hat{\mathbf{r}}_x, \hat{\mathbf{r}}_y, \hat{\mathbf{r}}_z, d_h \hat{\mathbf{r}}_x^2, d_h \hat{\mathbf{r}}_y^2, d_h \hat{\mathbf{r}}_z^2, 2d_h \hat{\mathbf{r}}_x \hat{\mathbf{r}}_y, 2d_h \hat{\mathbf{r}}_x \hat{\mathbf{r}}_z, 2d_h \hat{\mathbf{r}}_y \hat{\mathbf{r}}_z\}. \quad (10)$$

where the true comoving distance d_h of a galaxy is given by

$$d_h(z_h) = \frac{c}{H_0} \int_0^{z_h} \frac{dz'}{\sqrt{\Omega_m(1+z_h)^3 + \Omega_\Lambda}}, \quad (11)$$

and where z_h is the Hubble recessional redshift of that galaxy. H_0 is the Hubble constant of present-day Universe. Ω_m and Ω_Λ are the matter and dark energy densities of present-day Universe, respectively.

4.2. Bulk and shear moments estimator

Measuring cosmic flows can provide us with an intuitive understanding of the amplitude and direction of the measured (not the modeled or reconstructed) velocity field. In addition, comparing the measured U_p to the Λ CDM prediction enables us to test whether Λ CDM accurately describe the motion of galaxies in the nearby Universe. To avoid the non-Gaussianity of the peculiar velocities, we use the so-called η MLE (Nusser & Davis 1995, 2011; Qin et al. 2018, 2019b) to estimate the nine moment components U_p from the full sky galaxy catalogue CF4TF.

Assuming the log-distance ratio of the n -th galaxy, η_n have Gaussian errors ϵ_n , then the Gaussian likelihood function of a set of N galaxies can be written as (Nusser & Davis 1995, 2011; Qin et al. 2018, 2019b)

$$P(U_p, \epsilon_\star) = \prod_{n=1}^N \frac{1}{\sqrt{2\pi(\epsilon_n^2 + \epsilon_{\star,n}^2)}} \exp\left(-\frac{1}{2} \frac{(\eta_n - \tilde{\eta}_n(U_p))^2}{\epsilon_n^2 + \epsilon_{\star,n}^2}\right), \quad (12)$$

where the intrinsic scatter of the log-distance ratio ϵ_\star arises from the non-linear motions of the galaxies. We set it as a free parameter to fit.

Following the steps of the second paragraph in Section 4.1 of Qin et al. 2019b, the modeled log-distance ratio $\tilde{\eta}_n(U_p)$ of the n -th galaxy is converted by firstly substituting Eq. 8 into the usual peculiar velocity estimator (Colless et al. 2001; Hui & Greene 2006; Davis & Scrimgeour 2014; Scrimgeour et al. 2016; Qin et al. 2018, 2019b)

$$v = c \left(\frac{z - z_h}{1 + z_h} \right), \quad (13)$$

to replace v to calculate $d_h(U_p)$. Then we can calculate $\tilde{\eta}_n(U_p)$ from $d_h(U_p)$ and the observed redshift z of that galaxy.

We choose flat priors for the 10 independent parameters. For the three bulk flow components, we use flat priors in the interval $B_i \in [-1200, 1200]$ km s⁻¹. For the six shear components, we use flat priors in the interval $Q_{ij} \in [-100, 100]$ h km s⁻¹ Mpc⁻¹. We use flat priors in the interval $\epsilon_\star \in [-1000, 1000]$ h km s⁻¹ Mpc⁻¹ for ϵ_\star . Combining these flat priors with the likelihood in Eq.12 to obtain the posterior, then we use the Metropolis-Hastings Markov chain Monte Carlo⁵ (MCMC) algorithm to estimate the parameters.

The measurement error of the bulk flow component, e_{B_i} ($i = x, y, z$) is calculated from the standard deviation of the MCMC samples of the corresponding MCMC chain. They can be converted to the error of the bulk flow amplitude, e_B using (Scrimgeour et al. 2016; Qin et al. 2018):

$$e_B^2 = J C_{ij} J^T, \quad (i = 1, 2, 3), \quad (14)$$

where J is the Jacobian $\partial B / \partial B_i$. The covariance of the bulk flow components C_{ij} is computed using the MCMC samples.

4.3. Testing on mocks

To explore how well the estimator recover the true moments, we test it using mocks (comparison between data and cosmological models is presented in Section 5). The true moment $U_{p,t}$ of the mocks is defined as the weighted average

of the true velocities of the galaxies

$$U_{p,t} = \sum_{n=1}^N w_{p,n} \mathbf{v}_{n,t} \cdot \hat{\mathbf{r}}_n, \quad (15)$$

where $\mathbf{v}_{n,t}$ is the true velocity of the n -th galaxy and is known from the simulation, $\hat{\mathbf{r}}_n$ is the unit vector point to that galaxy. The weights are calculated using the mode function Eq.10, given by

$$w_{p,n} = \sum_{q=1}^9 A_{pq}^{-1} \frac{g_{q,n}}{\alpha_n^2 + \alpha_\star^2}, \quad A_{pq} = \sum_{n=1}^N \frac{g_{p,n} g_{q,n}}{\alpha_n^2 + \alpha_\star^2}, \quad (16)$$

where α_n is given by (Hui & Greene 2006; Johnson et al. 2014; Adams & Blake 2017):

$$\alpha_n = \frac{\ln(10) c z_n}{1 + z_n} \epsilon_n, \quad (17)$$

which is the measurement error of peculiar velocity. α_\star is converted from ϵ_\star using the similar expression.

Fig.6 shows the bulk (top panels) and shear moments (middle and bottom panels) measured from the mocks under equatorial coordinates. The error bars are the measurement errors calculated using the MCMC samples, and hence include the effect of peculiar velocity measurement errors, but not cosmic variance. The impact of cosmic variance can instead be inferred from the spread in true bulk flows between mock catalogues. When comparing our results to cosmological models in Section 5, we include both measurement errors *and* cosmic variance. 1000 example mocks are shown here. The black dashed lines are the expected one-to-one relation. The colored solid lines are the best fit to the co-responding colored points (moments). The best fit lines are almost consistent with the one-to-one relation, indicating the η MLE can recover the true moments. The slopes of the dashed lines are slightly different from the one-to-one relation. The reason for this is most likely due to we assume that the cosmic flow field is represented simply as bulk and shear moments, without higher order components. We leave testing of this hypothesis for future work since accurate measurements of higher moments need both larger numbers of galaxies and more isotropic and homogeneous sky coverage of galaxies.

The reduced χ^2 between the measured moments and true moments is given by

$$\chi_{\text{red}}^2 = \frac{1}{9 \times 1000 - 1} (\mathbf{U}_m - \mathbf{U}_t) \mathbf{C}^{-1} (\mathbf{U}_m - \mathbf{U}_t)^T, \quad (18)$$

where the measured moments \mathbf{U}_m and the true moments \mathbf{U}_t contain 9000 elements (1000 mocks times 9 moments), respectively. \mathbf{C} is the covariance matrix. Eq.8 gives the nine moments U_p as the components of the cosmic flow field. Since these moments are all being measured from a single

⁵ The PYTHON package emcee (Foreman-Mackey et al. 2013) is used.

observation location, and with incomplete sky-coverage, uncertainty of the measurement of one of these moments will be correlated with those of another, and this is true for all moments. C is a 9000×9000 matrix with $1000 \times 9 \times 9$ diagonal blocks and zero elsewhere. The 1000 diagonal blocks are calculated from the MCMC chains. The $\chi_{red}^2 = 1.806$. This slightly larger value of χ_{red}^2 is due to the intrinsic scatter between the measured moments and true moments, which is arise from the intrinsic scatter of the peculiar velocities α_* (or ϵ_* of log-distance ratio). α_* (or ϵ_*) is to encapsulate the non-linear peculiar motions of galaxies. The peculiar velocity estimator Eq.13 is not good enough to account for the non-linear peculiar motions. Therefore a more robust peculiar velocity estimator need to be developed in future work.

5. RESULTS AND DISCUSSION

5.1. Results and comparing to Λ CDM prediction

Applying η MLE to the real CF4TF data, we obtain the measured bulk and shear moments in the local Universe, as presented in Table 2. The moments are measured under Galactic coordinates. Fig.7 shows the 2D contours and histograms of the MCMC samples of the moments. The shaded areas of the histograms indicate the 1σ errors of the moments. To compare to theory, the characteristic scale of cosmic flow measurement is defined as (Scrimgeour et al. 2016)

$$d_{MLE} = \frac{\sum |d_{h,n}| W_n}{\sum W_n}, \quad (19)$$

where the weight factors $W_n = 1/(\alpha_n^2 + \alpha_*^2)$.

The Λ CDM predicted moments should have zero mean and ‘cosmic root mean square’ (CRMS) variation (Feldman et al. 2010). The CRMS is calculated from the following equation (Feldman et al. 2010; Ma et al. 2011; Johnson et al. 2014)

$$R_{pq}^v = \frac{\Omega_m^{1.1} H_0^2}{2\pi^2} \int \mathcal{W}_{pq}^2(k) \mathcal{P}(k) dk, \quad (20)$$

where the matter density power spectrum $\mathcal{P}(k)$ is generated using the CAMB package (Lewis et al. 2000). The window function is given by (Feldman et al. 2010; Ma et al. 2011; Johnson et al. 2014):

$$\mathcal{W}_{pq}^2(k) = \sum_{m,n}^N w_{p,m} w_{q,n} f_{mn}(k). \quad (21)$$

where $f_{mn}(k)$ is given by (Ma et al. 2011; Johnson et al. 2014)

$$f_{mn}(k) = \frac{1}{3} [j_0(kD_{mn}) - 2j_2(kD_{mn})] \hat{\mathbf{r}}_m \cdot \hat{\mathbf{r}}_n + \frac{1}{D_{mn}^2} j_2(kD_{mn}) r_m r_n \sin^2(\alpha_{mn}), \quad (22)$$

and where $D_{mn} \equiv |\mathbf{r}_m - \mathbf{r}_n|$ and $\alpha_{mn} = \cos^{-1}(\hat{\mathbf{r}}_m \cdot \hat{\mathbf{r}}_n)$. \mathbf{r}_n is the position vector of the n -th galaxy. $j_0(x)$ and $j_2(x)$ are the

Table 2. The bulk and shear moments measured from the CF4TF data. To compare to Λ CDM prediction, we also list the CRMS in the last column. The number of degrees of freedom is 9.

	η MLE	CRMS
B_x (km s ⁻¹)	175.9 ± 23.5	± 173.4
B_y (km s ⁻¹)	-330.2 ± 21.9	± 175.1
B_z (km s ⁻¹)	-38.9 ± 17.1	± 183.5
Q_{xx} (h km s ⁻¹ Mpc ⁻¹)	2.53 ± 0.74	± 2.62
Q_{xy} (h km s ⁻¹ Mpc ⁻¹)	-3.58 ± 0.58	± 1.70
Q_{xz} (h km s ⁻¹ Mpc ⁻¹)	1.52 ± 0.43	± 1.43
Q_{yy} (h km s ⁻¹ Mpc ⁻¹)	2.14 ± 0.79	± 3.65
Q_{yz} (h km s ⁻¹ Mpc ⁻¹)	0.47 ± 0.51	± 1.77
Q_{zz} (h km s ⁻¹ Mpc ⁻¹)	-1.16 ± 0.48	± 2.72
χ^2	10.4	
p -value	0.319	
Direction of bulk flow	$l=298.4 \pm 3.4^\circ$, $b=-5.9 \pm 2.7^\circ$	
d_{MLE} (h^{-1} Mpc)	35	

0th- and 2nd-order spherical Bessel function of the first kind. The weight factors are given by Eq.16.

Fig.8 shows the $p = q$ components of the window function W_{pq}^2 of the CF4TF data under Galactic coordinates. In Table 2, we list the CRMS predicted by Λ CDM. As shown in the top panel of Fig.8, the amplitudes of window functions for the three bulk flow components are similar, therefore, the co-responding CRMS of the three bulk flow components are similar in Table 2. As shown in the middle and bottom panels of Fig.8, the window functions for the y direction related components [Q_{yy} , Q_{xy} , Q_{yz}] have larger amplitudes, indicating larger cosmic variance in this direction. This is due to the an-isotropic sky coverage caused by the denser region contributed by ALFALFA galaxies. Therefore, in Table 2, the CRMS for the y direction related components, especially Q_{yy} , are larger than other shear moments components.

The Λ CDM predicted moments should have zero mean. Therefore, the χ^2 between the 9 measured moments and Λ CDM prediction is given by:

$$\chi^2 = U_p (C_{pq} + R_{pq}^v)^{-1} U_p^T. \quad (23)$$

where C_{pq} is the covariance of measurement errors, it is calculated from the MCMC samples. The $\chi^2 = 10.4$, and the corresponding p -value is 0.319, indicating the measurements are consistent with the Λ CDM prediction.

5.2. Comparing to other literature

To visualise the comparison of different bulk flow measurements from other surveys on a single figure, we need to standardise the window function due to the differing geometries and depths of the surveys. In this work, we use the spherical top-hat window function:

$$\mathcal{W}(k) = 3(\sin kR - kR \cos kR)/(kR)^3. \quad (24)$$

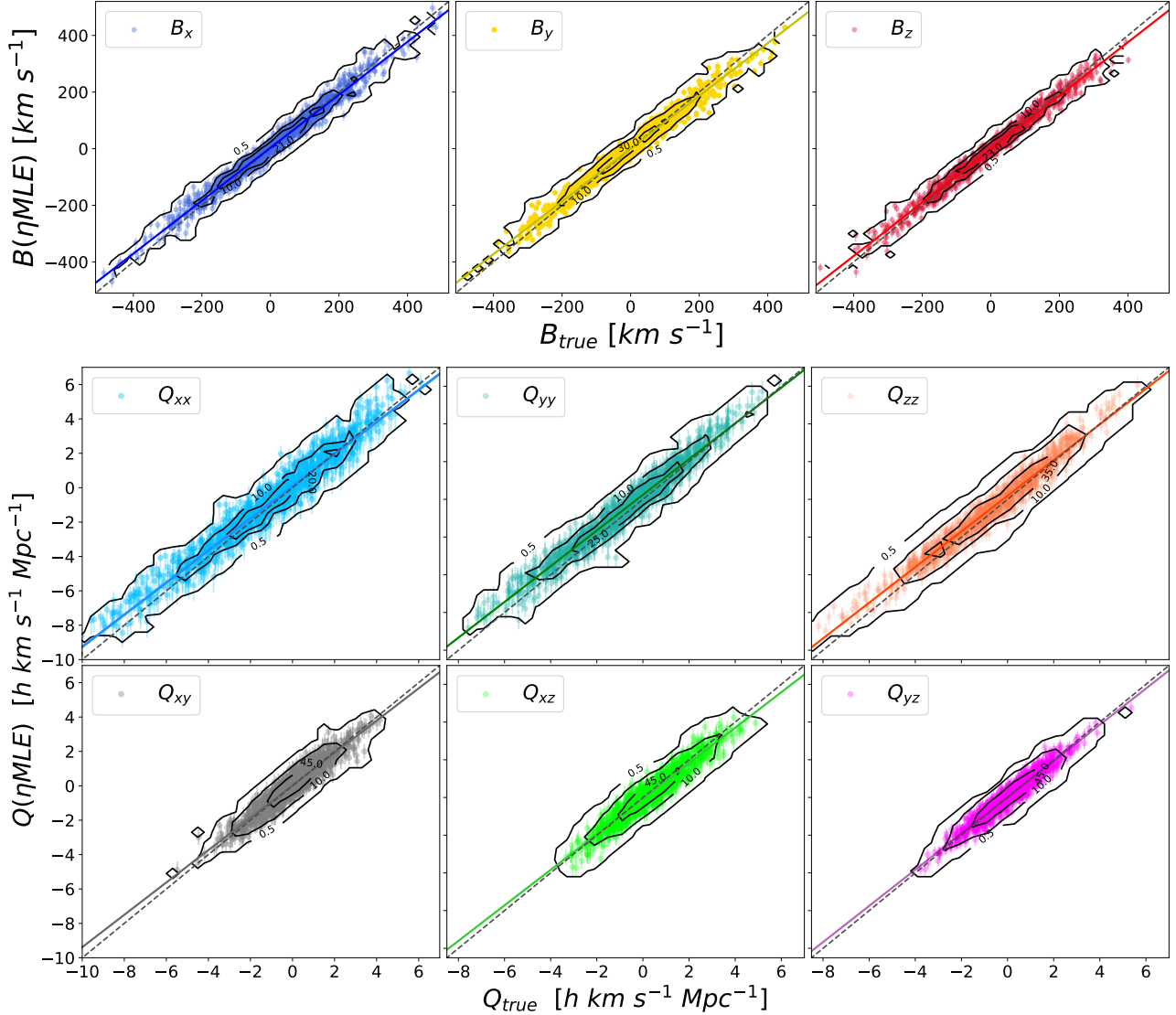


Figure 6. Comparing the measured bulk flow velocities (top panels) and shear moments (middle and bottom panels) of CF4TF mocks to the true moments. Measured under equatorial coordinates. 1000 example mocks are shown. The black dashed lines are the expected one-to-one relations. The colored solid lines are the best fit to the co-responding colored point. The contour indicates the 2D histogram of the dots. The numbers on the contour are the average numbers of the dots on the contour lines.

The other surveys we will compare are: W09: Watkins et al. (2009); C11: Colin et al. (2011); D11: Dai et al. (2011); N11: Nusser & Davis (2011); T12: Turnbull et al. (2012); M13: Ma & Scott (2013); H14: Hong et al. (2014); S16: Scrimgeour et al. (2016); Q18: Qin et al. (2018); Q19: Qin et al. (2019b); B20: Boruah et al. (2020); S21: Stahl et al. (2021).

In Fig.9, the pink curve is the Λ CDM prediction calculated from the spherical top-hat window function. The shade areas indicates the 1σ and 2σ cosmic variance. The yellow stars are the measurements from other surveys. The red dot is our measurement using CF4TF. Following the arguments in Scrimgeour et al. 2016, to be comparable to the top-hat window function prediction, we plot the W09 and

T12 measurements at twice their quoted depth since they have Gaussian windows. S16 measures the bulk flow from the 6dFGSv data (Springob et al. 2014), which is a hemispherical top-hat. Following the arguments in S16, we plot their measurement at effective radius $R_{\text{eff}} = (R^3/2)^{1/3}$. Q18 revised the bulk flow measurement of 6dFGSv by calibrating a bias in the Malmquist bias correction of 6dFGSv distance measurements, the revised result is show in Q18-6dFGSv. Generally, most of the measurements are consistent with the Λ CDM prediction, while the W09 does not agree with the Λ CDM prediction.

Comparing to other measurements (yellow stars), our measurement (red dot) has smaller error. B20 has smallest error bar, they measure bulk flow by comparing the reconstructed

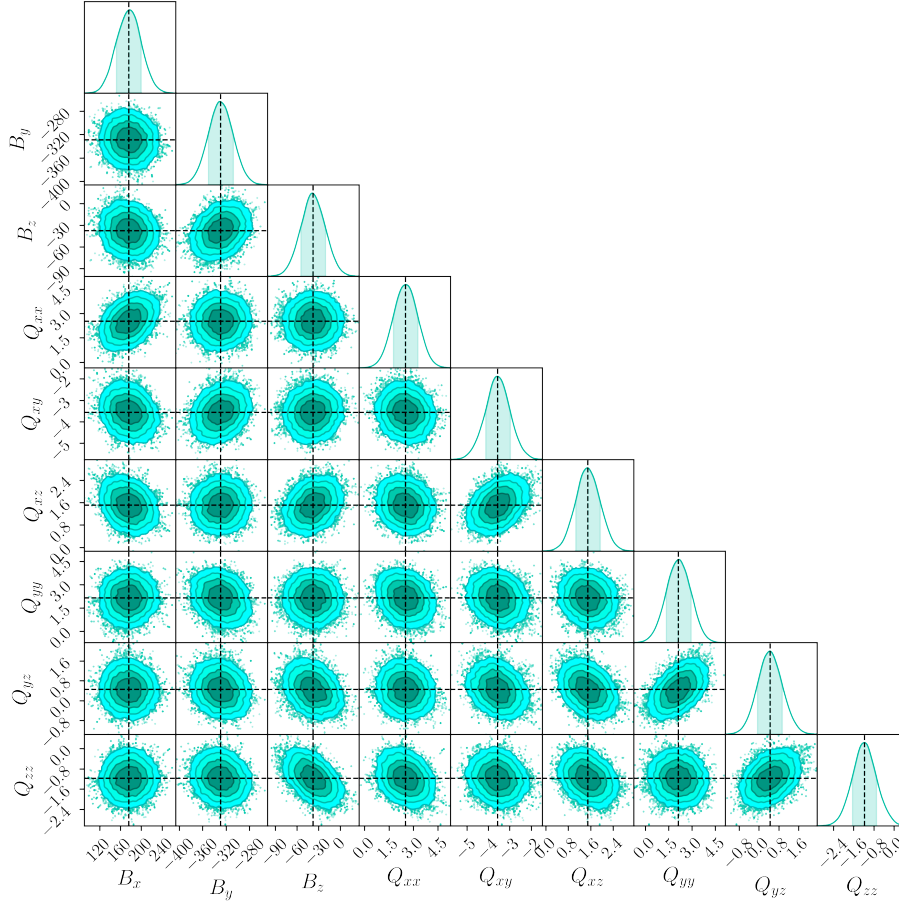


Figure 7. The 2D contours and the marginalised histograms of the MCMC samples of the bulk and shear moments. The shade areas in the histograms indicates the 68% confidence level of the moments.

velocity field of 2M++ (Carrick et al. 2015) to the measured velocity field of 465 supernovas. However, as presented in Section 5.1 of Carrick et al. 2015, the reconstructed field has many potential systematic effects which are hard to test. Q19 measures the bulk flow using Cosmicflows-3 catalogue (Tully et al. 2016) which contains 391 Type Ia supernovas, therefore, has smaller error bar too. However, the major part of the published Cosmicflows-3 catalogue is the 6dFGSv, which has not perfect Malmquist bias correction (Qin et al. 2018), therefore this measurement has potential systematic errors.

Fig.10 shows directions of bulk flows measured from different surveys under Galactic coordinates. The S16 measurements is significantly biased from other surveys. The revised result is show in Q18-6dFGSv.

6. CONCLUSION

In this paper, we present the mock sampling algorithm of CF4TF data. These mocks can realize the luminosity selection, survey geometry and clustering of the real CF4TF data. A combination of these CF4TF mocks and 6dFGSv mocks (Qin et al. 2018, 2019a) provide us with the mock catalogues for the two largest subsets of the final full Cosmicflows-4 cat-

alogue. The mocks can be used to further study cosmology in future work. For example, estimating the covariance matrix and errors of power spectrum and two-point correlation of velocities. The mock catalogues underlying this article will be shared on a reasonable request to the corresponding author.

We use mocks to test the cosmic flow estimator η MLE, we find that the estimator works well to recovers the true moments. We measure the bulk and shear moments of the local Universe using the CF4TF data. We find that the bulk flow in the local Universe is 376 ± 23 (error) ± 183 (cosmic variance) km s^{-1} at depth 35 Mpc h^{-1} , to the Galactic direction of $(l, b) = (298 \pm 3^\circ, -6 \pm 3^\circ)$. Both the measured bulk and shear moments are consistent with the Λ cold dark matter model prediction.

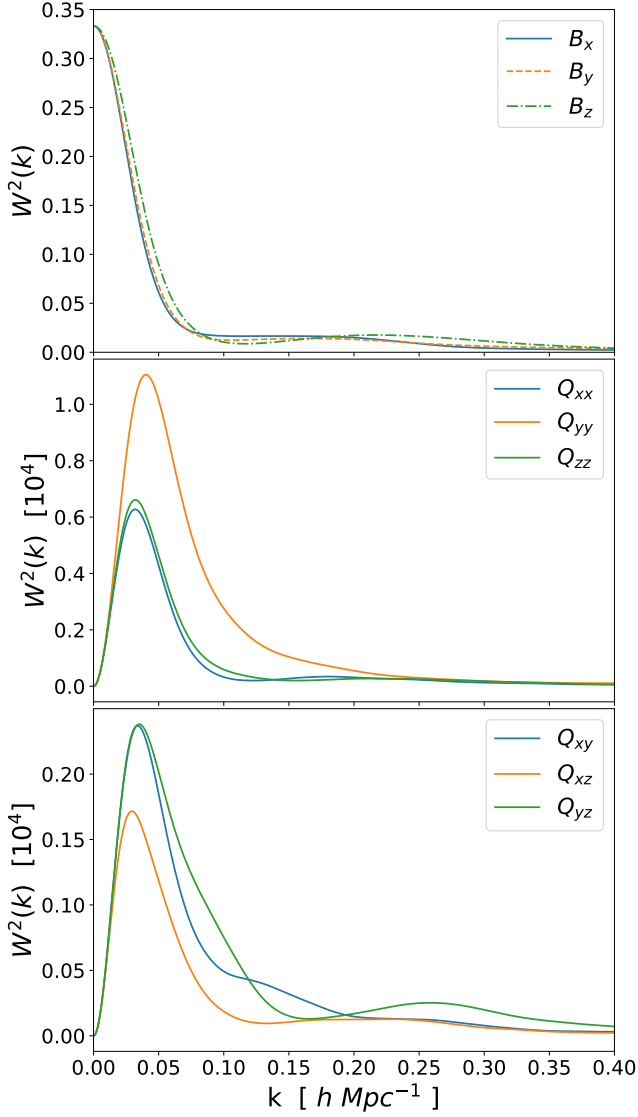


Figure 8. The window functions for CF4TF under Galactic coordinates. The top panels are for the bulk flow components. The middle panels are for the diagonal elements of the shear moments. The bottom panels are for the off-diagonal elements of the shear moments.

ACKNOWLEDGMENTS

FQ and DP are supported by the project 우주거대구조를 이용한 암흑우주 연구 (“Understanding Dark Universe Using Large Scale Structure of the Universe”), funded by the Ministry of Science. CH and KS are supported by the Australian Government through the Australian Research Council’s Laureate Fellowship funding scheme (project FL180100168).

Facilities: The L-PICOLA simulation and CF4TF mock sampling algorithm were performed on the OzSTAR national facility at Swinburne University of Technology. The Cosmicflows-4 Tully-Fisher catalogue is downloaded from the Extragalactic Distance Database (EDD) <http://edd.ifa.hawaii.edu/>.

Software: EMCEE (Foreman-Mackey et al. 2013), CHAIN-CONSUMER (Hinton 2016), SCIPY (Virtanen et al. 2020), MATPLOTLIB (Hunter 2007), HEALPIX (Zonca et al. 2019; Górski et al. 2005).

APPENDIX

A. I-BAND LUMINOSITY FUNCTION

In the CF4TF catalogue, we have the fully corrected ⁶ i , g , r , z , w_1 and w_2 bands apparent magnitudes. However, non of these bands are for all galaxies. To fit the luminosity function of all CF4TF galaxies, we need to work out a single band of magnitudes for all galaxies.

⁶ The corrections are done for Milky Way obscuration, redshiftk-correction, and aperture effects and global dust obscuration (Kourkchi et al. 2020b).

There are 6776 galaxies have i -band apparent magnitudes m_i , while 5037 galaxies have w_1 -band apparent magnitudes m_{w_1} . There are 2033 galaxies have both w_1 -band and i -band apparent magnitudes in the CF4TF catalogue. Following the arguments in Kourkchi et al. 2020b, we can firstly calculate the differences between the magnitudes of the two bands for these common galaxies, $\Delta_{i,w_1} = m_i - m_{w_1}$. Then using the equation shown in Figure 15 of Kourkchi et al. 2019 to convert the w_2 -band main principal components P_{1,w_2} to w_1 -band main principal components P_{1,w_1} . Finally, following

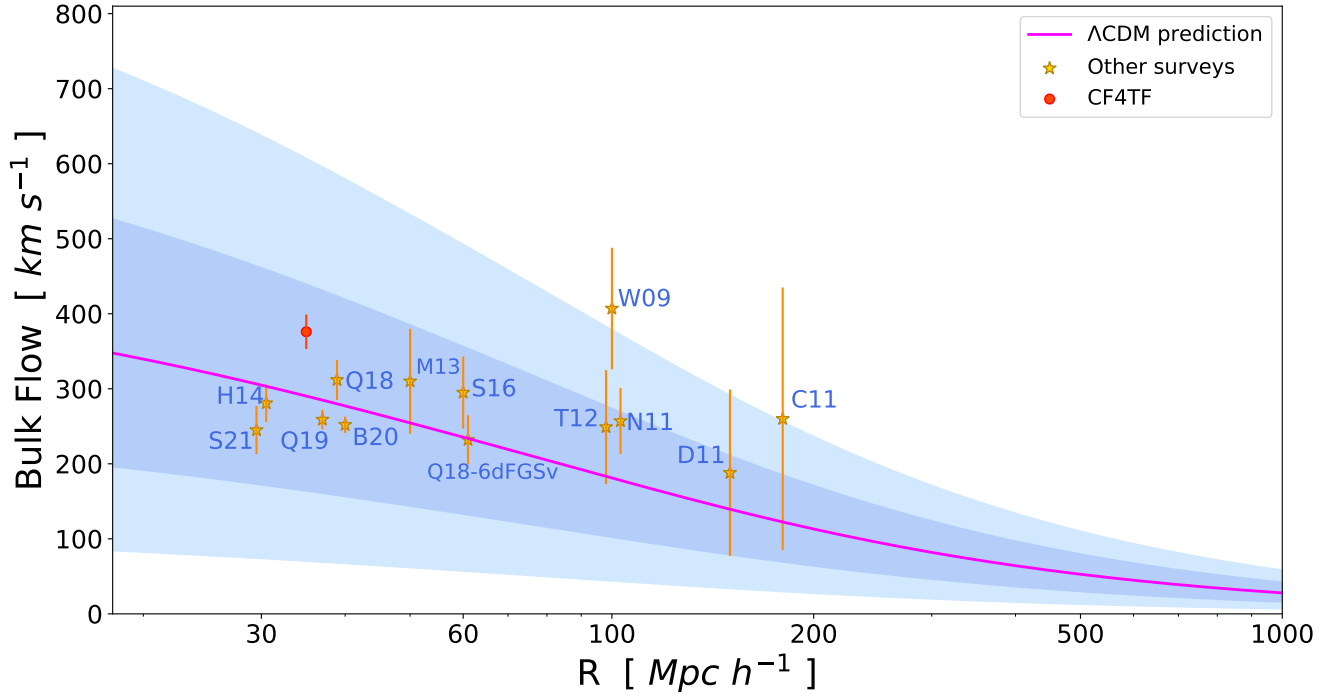


Figure 9. Comparing the bulk flow measurements from different surveys: W09: Watkins et al. (2009); C11: Colin et al. (2011); D11: Dai et al. (2011); N11: Nusser & Davis (2011); T12: Turnbull et al. (2012); M13: Ma & Scott (2013); H14: Hong et al. (2014); S16: Scrimgeour et al. (2016); Q18: Qin et al. (2018); Q19: Qin et al. (2019b); B20: Boruah et al. (2020); S21: Stahl et al. (2021). The pink curve is the Λ CDM prediction calculated from the spherical top-hat window function. The shade areas indicates the 1σ and 2σ cosmic variance. The yellow stars are the measurements from other surveys. The red dot is our measurement using CF4TF.

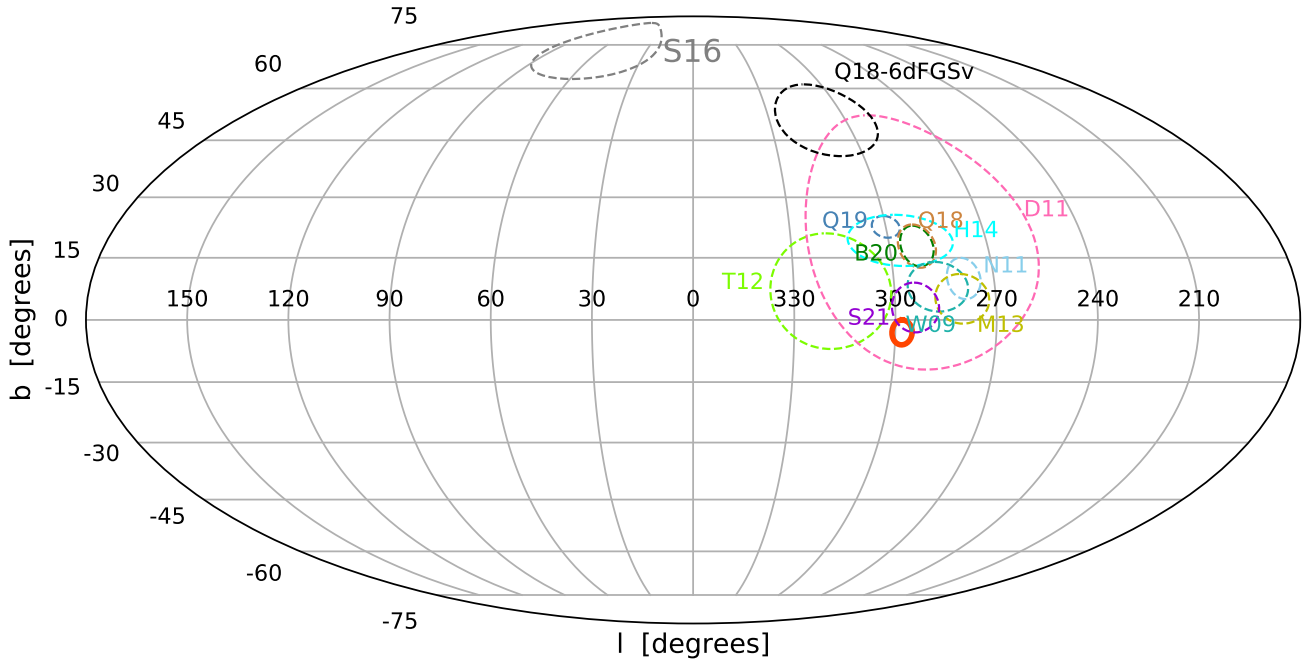


Figure 10. Comparing the bulk flow direction from different surveys under Galactic coordinates: W09: Watkins et al. (2009); D11: Dai et al. (2011); N11: Nusser & Davis (2011); T12: Turnbull et al. (2012); M13: Ma & Scott (2013); H14: Hong et al. (2014); S16: Scrimgeour et al. (2016); Q18: Qin et al. (2018); Q19: Qin et al. (2019b); B20: Boruah et al. (2020); S21: Stahl et al. (2021). The red solid circle is our measurement using CF4TF. The size of the circles indicate the 1σ error of the measurements.

the arguments in Appendix B4 of [Kourkchi et al. 2020b](#), we using the Random Forest Regressor from the Python package `SCIKIT-LEARN` to obtain the w_1 -band apparent magnitudes of all CF4TF galaxies.

Since the i -band magnitude cut is the commonly quoted one in the previous literature ([Kourkchi et al. 2019, 2020b,a](#)), we then need to convert w_1 -band magnitudes to i -band magnitudes. The blue dots in Fig.11 shows the relation between the i -band apparent magnitudes and w_1 -band apparent magnitudes of the 6776 galaxies. Then using Random Forest Regressor to obtain the i -band apparent magnitudes of the rest galaxies, as shown in the yellow dots in Fig.11. Thus, we obtain the i -band apparent magnitudes for all CF4TF galaxies. Converting the i -band apparent magnitudes to absolute magnitudes using the distance modulus data in the CF4TF catalogue. The distribution of i -band absolute magnitudes M_i is shown in the bottom panel of Fig.12.

To generate mock catalogues for CF4TF, we need to fit the i -band luminosity function for the data. We use the Schechter function ([Schechter 1976](#))

$$\phi(M_i) = 0.4 \ln(10) \phi_\star 10^{-0.4(M_i - M_\star)(\alpha + 1)} \exp \left[-10^{-0.4(M_i - M_\star)} \right]. \quad (\text{A1})$$

The best fit values of parameters M_\star and α are give in the Table 6 of [Kourkchi et al. 2020a](#). However, the shape of the luminosity function given by their parameters can not match the measurements, see the green curve in the top panel of Fig.12. In addition, [Kourkchi et al. 2020a](#) does not provide the normalization parameter ϕ_\star of the luminosity function. Therefore, instead of using the values in Table 6 of [Kourkchi et al. 2020a](#), we fit our own luminosity function. The best fitted values are $M_\star = -21.528^{+0.030}_{-0.029}$ and $\alpha = -0.280^{+0.020}_{-0.018}$. The fit result is shown in the blue curve in the top panel of Fig.12.

To emphasize, in this stage we only want to know the shape parameters of the luminosity function, i.e. we only want to know the values of M_\star and α . While the normalization parameter ϕ_\star will be fitted in Section 3 since it is difficult to obtain the survey volume of CF4TF due to the complex survey geometry.

B. THE FIVE CF4TF PATCHES

In building our mock catalogues, we treat the inhomogeneous CF4TF data as consisting of 5 distinct patches, each of which has their own unique redshift distribution. Fig.13 shows the five patches of the CF4TF sky coverage we use, which are defined as, and correspond to:

1. The blue region: $0^\circ < \text{Dec} < 38^\circ$ and $111^\circ < \text{R.A.} < 250^\circ$. Covers the ALFALFA data in the northern Galactic region.

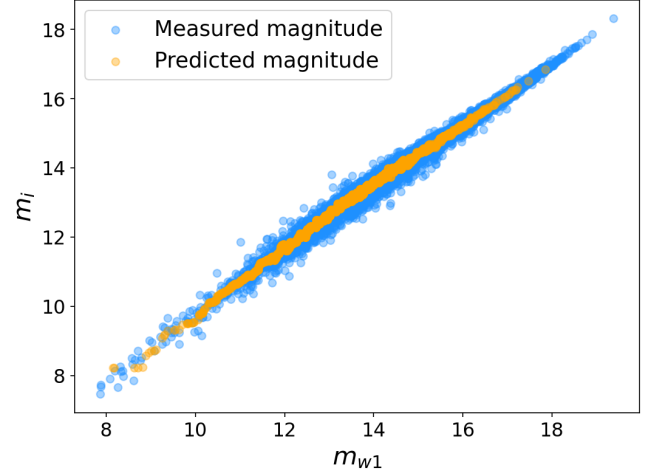


Figure 11. The relation between the i -band apparent magnitudes and w_1 -band apparent magnitudes of CF4TF.

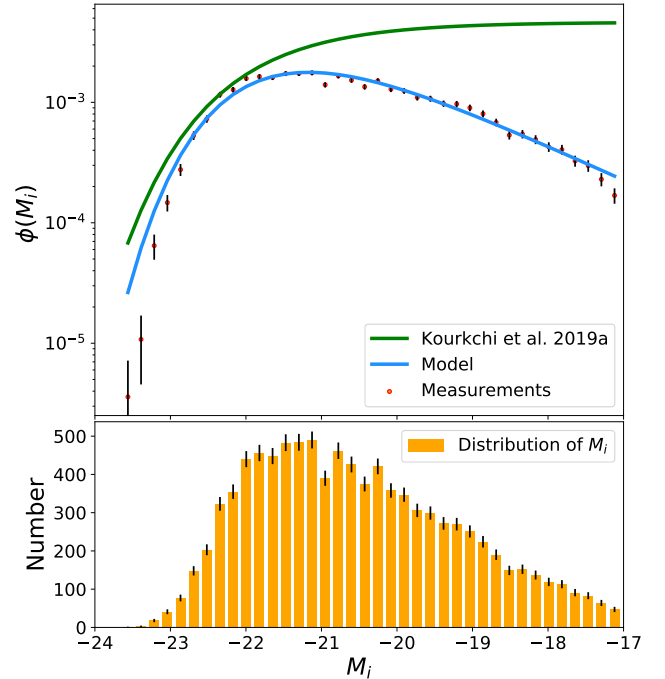


Figure 12. The bottom panel shows the histogram of the i -band absolute magnitude. The top panel are the corresponding luminosity function. The blue curve is the Schechter model fit to the data. The green curve is the Schechter model given by [Kourkchi et al. 2020a](#).

2. The black region: $0^\circ < \text{Dec} < 38^\circ$ and $0^\circ < \text{R.A.} < 48^\circ$ and $325.5^\circ < \text{R.A.} < 360^\circ$. Covers the ALFALFA data in the southern Galactic region
3. The green region: $\text{Dec} > -45^\circ$. Relatively uniform galaxies, mainly from ADHI, with additions from the Springob/Cornell and Pre-Digital HI catalogues.

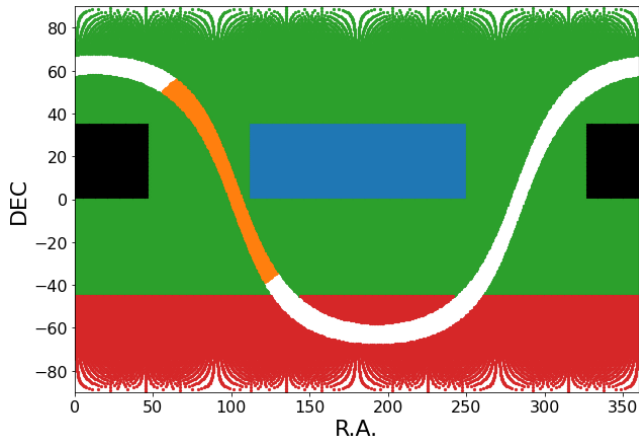


Figure 13. The five non-overlapping patches of the CF4TF sky coverage we adopt for producing our mock catalogues.

4. The orange region: $149^\circ < l < 255^\circ$ and $-5^\circ < b < 5^\circ$. Sparse data in the Galactic plane from ADHI, the Springob/Cornell and Pre-Digital HI catalogues, where Galactic extinction reduces the number density of observed TF objects.

5. The red region: $\text{Dec} < -45^\circ$. Mainly galaxies from the ADHI but observed using the Parkes Telescope, which results in a lower number density of these galaxies relative to the green region.

REFERENCES

- Adams, C., & Blake, C. 2017, *MNRAS*, 471, 839, doi: [10.1093/mnras/stx1529](https://doi.org/10.1093/mnras/stx1529)
- Bianchi, D., Gil-Marín, H., Ruggeri, R., & Percival, W. J. 2015, *MNRAS*, 453, L11, doi: [10.1093/mnras/slv090](https://doi.org/10.1093/mnras/slv090)
- Blot, L., Crocce, M., Sefusatti, E., et al. 2019, *MNRAS*, 485, 2806, doi: [10.1093/mnras/stz507](https://doi.org/10.1093/mnras/stz507)
- Boruah, S. S., Hudson, M. J., & Lavaux, G. 2020, *MNRAS*, 498, 2703, doi: [10.1093/mnras/staa2485](https://doi.org/10.1093/mnras/staa2485)
- Carrick, J., Turnbull, S. J., Lavaux, G., & Hudson, M. J. 2015, *MNRAS*, 450, 317, doi: [10.1093/mnras/stv547](https://doi.org/10.1093/mnras/stv547)
- Colin, J., Mohayaee, R., Sarkar, S., & Shafieloo, A. 2011, *MNRAS*, 414, 264, doi: [10.1111/j.1365-2966.2011.18402.x](https://doi.org/10.1111/j.1365-2966.2011.18402.x)
- Colless, M., Saglia, R. P., Burstein, D., et al. 2001, *MNRAS*, 321, 277, doi: [10.1046/j.1365-8711.2001.04044.x](https://doi.org/10.1046/j.1365-8711.2001.04044.x)
- Conroy, C., Wechsler, R. H., & Kravtsov, A. V. 2006, *ApJ*, 647, 201, doi: [10.1086/503602](https://doi.org/10.1086/503602)
- Courtois, H. M., Tully, R. B., Fisher, J. R., et al. 2009, *AJ*, 138, 1938, doi: [10.1088/0004-6256/138/6/1938](https://doi.org/10.1088/0004-6256/138/6/1938)
- Courtois, H. M., Tully, R. B., Makarov, D. I., et al. 2011, *MNRAS*, 414, 2005, doi: [10.1111/j.1365-2966.2011.18515.x](https://doi.org/10.1111/j.1365-2966.2011.18515.x)
- Dai, D.-C., Kinney, W. H., & Stojkovic, D. 2011, *Journal of Cosmology and Astro-Particle Physics*, 2011, 015, doi: [10.1088/1475-7516/2011/04/015](https://doi.org/10.1088/1475-7516/2011/04/015)
- Davis, T. M., & Scrimgeour, M. I. 2014, *MNRAS*, 442, 1117, doi: [10.1093/mnras/stu920](https://doi.org/10.1093/mnras/stu920)
- Djorgovski, S., & Davis, M. 1987, *ApJ*, 313, 59, doi: [10.1086/164948](https://doi.org/10.1086/164948)
- Dressler, A., Lynden-Bell, D., Burstein, D., et al. 1987, *ApJ*, 313, 42, doi: [10.1086/164947](https://doi.org/10.1086/164947)
- Elahi, P. J. 2009, PhD thesis, Queen's University (Canada)
- Feldman, H. A., Kaiser, N., & Peacock, J. A. 1994, *ApJ*, 426, 23, doi: [10.1086/174036](https://doi.org/10.1086/174036)
- Feldman, H. A., & Watkins, R. 2008, *MNRAS*, 387, 825, doi: [10.1111/j.1365-2966.2008.13288.x](https://doi.org/10.1111/j.1365-2966.2008.13288.x)
- Feldman, H. A., Watkins, R., & Hudson, M. J. 2010, *MNRAS*, 407, 2328, doi: [10.1111/j.1365-2966.2010.17052.x](https://doi.org/10.1111/j.1365-2966.2010.17052.x)
- Fisher, J. R., & Tully, R. B. 1981, *ApJS*, 47, 139, doi: [10.1086/190755](https://doi.org/10.1086/190755)
- Foreman-Mackey, D., Hogg, D. W., Lang, D., & Goodman, J. 2013, *PASP*, 125, 306, doi: [10.1086/670067](https://doi.org/10.1086/670067)
- Górski, K. M., Hivon, E., Banday, A. J., et al. 2005, *ApJ*, 622, 759, doi: [10.1086/427976](https://doi.org/10.1086/427976)
- Haynes, M. P., Giovanelli, R., Martin, A. M., et al. 2011, *AJ*, 142, 170, doi: [10.1088/0004-6256/142/5/170](https://doi.org/10.1088/0004-6256/142/5/170)
- Haynes, M. P., Giovanelli, R., Kent, B. R., et al. 2018, *ApJ*, 861, 49, doi: [10.3847/1538-4357/aac956](https://doi.org/10.3847/1538-4357/aac956)
- Hinton, S. R. 2016, *The Journal of Open Source Software*, 1, 00045, doi: [10.21105/joss.00045](https://doi.org/10.21105/joss.00045)
- Hong, T., Springob, C. M., Staveley-Smith, L., et al. 2014, *MNRAS*, 445, 402, doi: [10.1093/mnras/stu1774](https://doi.org/10.1093/mnras/stu1774)
- Howlett, C. 2019, *MNRAS*, 487, 5209, doi: [10.1093/mnras/stz1403](https://doi.org/10.1093/mnras/stz1403)
- Howlett, C., Manera, M., & Percival, W. J. 2015a, *Astronomy and Computing*, 12, 109, doi: [10.1016/j.ascom.2015.07.003](https://doi.org/10.1016/j.ascom.2015.07.003)
- . 2015b, L-PICOLA: Fast dark matter simulation code, *Astrophysics Source Code Library*. <http://ascl.net/1507.004>
- Howlett, C., Ross, A. J., Samushia, L., Percival, W. J., & Manera, M. 2015c, *MNRAS*, 449, 848, doi: [10.1093/mnras/stu2693](https://doi.org/10.1093/mnras/stu2693)
- Howlett, C., Staveley-Smith, L., Elahi, P. J., et al. 2017, *MNRAS*, 471, 3135, doi: [10.1093/mnras/stx1521](https://doi.org/10.1093/mnras/stx1521)
- Huchtmeier, W. K., & Richter, O. G. 1989, *A General Catalog of HI Observations of Galaxies. The Reference Catalog*.
- Hui, L., & Greene, P. B. 2006, *PhRvD*, 73, 123526, doi: [10.1103/PhysRevD.73.123526](https://doi.org/10.1103/PhysRevD.73.123526)

- Hunter, J. D. 2007, *Computing in Science Engineering*, 9, 90, doi: [10.1109/MCSE.2007.55](https://doi.org/10.1109/MCSE.2007.55)
- Jaffe, A. H., & Kaiser, N. 1995, *ApJ*, 455, 26, doi: [10.1086/176551](https://doi.org/10.1086/176551)
- Jarrett, T. 2004, *PASA*, 21, 396, doi: [10.1071/AS04050](https://doi.org/10.1071/AS04050)
- Johnson, A., Blake, C., Koda, J., et al. 2014, *MNRAS*, 444, 3926, doi: [10.1093/mnras/stu1615](https://doi.org/10.1093/mnras/stu1615)
- Kaiser, N. 1988, *MNRAS*, 231, 149, doi: [10.1093/mnras/231.2.149](https://doi.org/10.1093/mnras/231.2.149)
- Knebe, A., Pearce, F. R., Lux, H., et al. 2013, *MNRAS*, 435, 1618, doi: [10.1093/mnras/stt1403](https://doi.org/10.1093/mnras/stt1403)
- Kourkchi, E., Tully, R. B., Anand, G. S., et al. 2020a, *ApJ*, 896, 3, doi: [10.3847/1538-4357/ab901c](https://doi.org/10.3847/1538-4357/ab901c)
- Kourkchi, E., Tully, R. B., Neill, J. D., et al. 2019, *ApJ*, 884, 82, doi: [10.3847/1538-4357/ab4192](https://doi.org/10.3847/1538-4357/ab4192)
- Kourkchi, E., Tully, R. B., Eftekharzadeh, S., et al. 2020b, *ApJ*, 902, 145, doi: [10.3847/1538-4357/abb66b](https://doi.org/10.3847/1538-4357/abb66b)
- Lavaux, G., Tully, R. B., Mohayaee, R., & Colombi, S. 2010, *ApJ*, 709, 483, doi: [10.1088/0004-637X/709/1/483](https://doi.org/10.1088/0004-637X/709/1/483)
- Lewis, A., Challinor, A., & Lasenby, A. 2000, *Astrophys. J.*, 538, 473, doi: [10.1086/309179](https://doi.org/10.1086/309179)
- Ma, Y.-Z., Gordon, C., & Feldman, H. A. 2011, *PhRvD*, 83, 103002, doi: [10.1103/PhysRevD.83.103002](https://doi.org/10.1103/PhysRevD.83.103002)
- Ma, Y.-Z., & Pan, J. 2014, *MNRAS*, 437, 1996, doi: [10.1093/mnras/stt2038](https://doi.org/10.1093/mnras/stt2038)
- Ma, Y.-Z., & Scott, D. 2013, *MNRAS*, 428, 2017, doi: [10.1093/mnras/sts178](https://doi.org/10.1093/mnras/sts178)
- Magoulas, C., Springob, C. M., Colless, M., et al. 2012, *MNRAS*, 427, 245, doi: [10.1111/j.1365-2966.2012.21421.x](https://doi.org/10.1111/j.1365-2966.2012.21421.x)
- Masters, K. L., Springob, C. M., & Huchra, J. P. 2008, *AJ*, 135, 1738, doi: [10.1088/0004-6256/135/5/1738](https://doi.org/10.1088/0004-6256/135/5/1738)
- Navarro, J. F., Frenk, C. S., & White, S. D. M. 1997, *ApJ*, 490, 493, doi: [10.1086/304888](https://doi.org/10.1086/304888)
- Nusser, A., & Davis, M. 1995, *MNRAS*, 276, 1391, doi: [10.1093/mnras/276.4.1391](https://doi.org/10.1093/mnras/276.4.1391)
- . 2011, *ApJ*, 736, 93, doi: [10.1088/0004-637X/736/2/93](https://doi.org/10.1088/0004-637X/736/2/93)
- Onions, J., Knebe, A., Pearce, F. R., et al. 2012, *MNRAS*, 423, 1200, doi: [10.1111/j.1365-2966.2012.20947.x](https://doi.org/10.1111/j.1365-2966.2012.20947.x)
- Parnovsky, S. L., Kudrya, Y. N., Karachentseva, V. E., & Karachentsev, I. D. 2001, *Astronomy Letters*, 27, 765, doi: [10.1134/1.1424358](https://doi.org/10.1134/1.1424358)
- Prada, F., Klypin, A. A., Cuesta, A. J., Betancort-Rijo, J. E., & Primack, J. 2012, *MNRAS*, 423, 3018, doi: [10.1111/j.1365-2966.2012.21007.x](https://doi.org/10.1111/j.1365-2966.2012.21007.x)
- Qin, F. 2021, arXiv e-prints, arXiv:2105.04800. <https://arxiv.org/abs/2105.04800>
- Qin, F., Howlett, C., & Staveley-Smith, L. 2019a, *MNRAS*, 487, 5235, doi: [10.1093/mnras/stz1576](https://doi.org/10.1093/mnras/stz1576)
- Qin, F., Howlett, C., Staveley-Smith, L., & Hong, T. 2018, *MNRAS*, 477, 5150, doi: [10.1093/mnras/sty928](https://doi.org/10.1093/mnras/sty928)
- . 2019b, *MNRAS*, 482, 1920, doi: [10.1093/mnras/sty2826](https://doi.org/10.1093/mnras/sty2826)
- Robotham, A. S. G., & Howlett, C. 2018, *Research Notes of the American Astronomical Society*, 2, 55, doi: [10.3847/2515-5172/aacc70](https://doi.org/10.3847/2515-5172/aacc70)
- Said, K., Colless, M., Magoulas, C., Lucey, J. R., & Hudson, M. J. 2020, *MNRAS*, 497, 1275, doi: [10.1093/mnras/staa2032](https://doi.org/10.1093/mnras/staa2032)
- Schechter, P. 1976, *ApJ*, 203, 297, doi: [10.1086/154079](https://doi.org/10.1086/154079)
- Scrimgeour, M. I., Davis, T. M., Blake, C., et al. 2016, *MNRAS*, 455, 386, doi: [10.1093/mnras/stv2146](https://doi.org/10.1093/mnras/stv2146)
- Springob, C. M., Haynes, M. P., Giovanelli, R., & Kent, B. R. 2005, *ApJS*, 160, 149, doi: [10.1086/431550](https://doi.org/10.1086/431550)
- Springob, C. M., Magoulas, C., Colless, M., et al. 2014, *MNRAS*, 445, 2677, doi: [10.1093/mnras/stu1743](https://doi.org/10.1093/mnras/stu1743)
- Stahl, B. E., de Jaeger, T., Boruah, S. S., et al. 2021, arXiv e-prints, arXiv:2105.05185. <https://arxiv.org/abs/2105.05185>
- Staveley-Smith, L., & Davies, R. D. 1989, *MNRAS*, 241, 787, doi: [10.1093/mnras/241.4.787](https://doi.org/10.1093/mnras/241.4.787)
- Strauss, M. A., & Willick, J. A. 1995, *PhR*, 261, 271, doi: [10.1016/0370-1573\(95\)00013-7](https://doi.org/10.1016/0370-1573(95)00013-7)
- Tassev, S., Zaldarriaga, M., & Eisenstein, D. J. 2013, *JCAP*, 2013, 036, doi: [10.1088/1475-7516/2013/06/036](https://doi.org/10.1088/1475-7516/2013/06/036)
- Tully, R. B., Courtois, H. M., & Sorce, J. G. 2016, *AJ*, 152, 50, doi: [10.3847/0004-6256/152/2/50](https://doi.org/10.3847/0004-6256/152/2/50)
- Tully, R. B., & Fisher, J. R. 1977, *A&A*, 54, 661
- Turnbull, S. J., Hudson, M. J., Feldman, H. A., et al. 2012, *MNRAS*, 420, 447, doi: [10.1111/j.1365-2966.2011.20050.x](https://doi.org/10.1111/j.1365-2966.2011.20050.x)
- Vale, A., & Ostriker, J. P. 2004, *MNRAS*, 353, 189, doi: [10.1111/j.1365-2966.2004.08059.x](https://doi.org/10.1111/j.1365-2966.2004.08059.x)
- Virtanen, P., Gommers, R., Oliphant, T. E., et al. 2020, *Nature Methods*, 17, 261, doi: [10.1038/s41592-019-0686-2](https://doi.org/10.1038/s41592-019-0686-2)
- Watkins, R., & Feldman, H. A. 2015, *MNRAS*, 450, 1868, doi: [10.1093/mnras/stv651](https://doi.org/10.1093/mnras/stv651)
- Watkins, R., Feldman, H. A., & Hudson, M. J. 2009, *MNRAS*, 392, 743, doi: [10.1111/j.1365-2966.2008.14089.x](https://doi.org/10.1111/j.1365-2966.2008.14089.x)
- Wright, E. L., Eisenhardt, P. R. M., Mainzer, A. K., et al. 2010, *AJ*, 140, 1868, doi: [10.1088/0004-6256/140/6/1868](https://doi.org/10.1088/0004-6256/140/6/1868)
- Yamamoto, K., Nakamichi, M., Kamino, A., Bassett, B. A., & Nishioka, H. 2006, *PASJ*, 58, 93, doi: [10.1093/pasj/58.1.93](https://doi.org/10.1093/pasj/58.1.93)
- York, D. G., Adelman, J., Anderson, John E., J., et al. 2000, *AJ*, 120, 1579, doi: [10.1086/301513](https://doi.org/10.1086/301513)
- Zonca, A., Singer, L., Lenz, D., et al. 2019, *Journal of Open Source Software*, 4, 1298, doi: [10.21105/joss.01298](https://doi.org/10.21105/joss.01298)